January 1994

Low Frequency Climate Variability: Understanding the Rise and Fall of the Great Salt Lake

Michael E. Mann

Upmanu Lall

Barry Saltzman

Low Frequency Climate Variability: Understanding the Rise and Fall of the Great Salt Lake

Michael E. Mann, Upmanu Lall, Barry Saltzman

Address list:

M. E. Mann* and B. Saltzman, Yale University, Department of Geology and Geophysics, Kline Geology Laboratory, P.O. Box 6666, New Haven, CT 06511-8130, U.S.A.

U. Lall, Utah Water Research Laboratory, Utah State University, Logan, UT 84322, U.S.A.

submitted to *Science*, August 1994

Connections between the Great Salt Lake (GSL) volume (V) and large-scale climate variations are developed through an analysis of the time series of the month-to-month differences in V (ΔV), local precipitation and streamflow, and gridded U.S. sea level pressure and global temperature data. We isolate decadal and secular modes of climate variability that are coherent with ΔV variations. The decadal variations result from a low-frequency north-south shifting of storm tracks which influence winter precipitation. These variations describe nearly 18% of the interannual variance in ΔV, while the secular trend accounts for only ~1.5%. The latter appears to arise from a combination of increased evaporation due to secular warming, and the influence of changes in atmospheric circulation on local precipitation, the combined effects of which largely cancel.

Forecasting hydrological systems requires an understanding of the long-term climate variability that drives them. Empirical analyses of hydroclimatic data that demonstrate the connection in space and time between hydrologic and climatic phenemena is a key step in this process. Several workers (1) have related large-scale atmospheric circulation to regional precipitation and streamflow patterns. This holds promise for relating *variability* in large-scale atmospheric circulation and hydrological conditions. Decadal and longer time-scale variations are particularly important for understanding drought and protracted wet periods. Here, we demonstrate that large-scale climatic variability may explain variations in the Great Salt Lake (GSL) volume (V) on these time scales.

The GSL, which is the fourth largest closed-basin saline lake in the world, provides an interesting case study because of its dramatic historical fluctuations (Fig. 1), and its emphasis of lower frequencies through a spatial and temporal integration of climatic processes. The location of GSL in a mountainous, semi-arid environment (Fig. 2) makes it sensitive to climatic signals. To clarify the connections between climatic variability and V, we analyze nearly century-long records of gridded U.S. sea level pressure (P_s), gridded global temperature anomalies, local precipitation (Silver Lake-Brighton-SLB) and streamflow (Blacksmith Fork at Hyrum-BFH), and V (2). We resolve such connections by identifying coherence between at-site hydrological processes and dominant spatiotemporal modes of climatic variability established through Singular Value Decomposition (SVD) of the gridded data in the frequency domain (3). Variations in large-scale P_s patterns reflect changes in atmospheric circulation that affect regional precipitation, and hence V. Temperature fluctuations associated with large-scale climatic variability may also influence V through their effect on evaporation. It is convenient to analyze the monthly-differenced V record (ΔV) rather than V itself, as the former responds more directly to precipitative and evaporative fluxes.

We concentrate on the decadal and secular time scales associated with statistically significant peaks in the SVD variance spectra of the the sea level pressure and temperature fields (Fig. 3). The sum of the secular and quasidecadal reconstructions

of ΔV (Fig. 4) explains roughly 20% of the total interannual variance in the record (4). Variability in at-site hydrology on these and interannual time scales is discussed elsewhere (5). Interannual variability in these records has been correlated with the El Nino/Southern Oscillation (ENSO) (6)

Decadal variability in atmospheric circulation (7), U.S. precipitation (8), and GSL volume specifically (9) has been associated with the $\sim$11 year sunspot cycle. We see (Fig. 5) that this is not a plausible explanation for the climatic variations observed in this study. Decadal signals nonetheless have been observed in a wide range of climatic fields, including gridded global surface temperature (10), North Atlantic sea level pressure, winds, and marine and air temperature (11), U.S. temperature (12), U.S. streamflow (13), and Great Basin precipitation (14). There is some evidence (10,11) that this variability has its origins in North Atlantic ocean-atmosphere interaction.

A consistent decadal time-scale signal is evident in our analysis. The quasidecadal variations in P_s are coherent (Fig. 6) with the corresponding global temperature variations (10) at $> 95\%$ confidence level (15). Quasidecadal variations in ΔV, SLB precipitation, BFH streamflow (4), are significantly correlated with each other, and anticorrelated with the local projection of the quasidecadal P_s mode (Fig. 7). Maximum ΔV occurs at roughly 6-10 month lag relative to peak precipitation, consistent with expectations of the time scales associated with snow accumulation, melt and runoff processes. The large-scale pattern (Fig. 8) coincident with these conditions indicates a low pressure anomaly from the Great Basin through the Gulf of Mexico. The low pressure anomaly in the Great Basin is related to an increased likelihood for the storm track to shift southward from its typical location to the north (e.g., Montana/Idaho) into the GSL region (16), leading to enhanced winter precipitation. The precipitation response is non-linearly related to the P_s variations because a small southward shift in the storm track enhances precipitation considerably. Note (Fig. 7) that the P_s fluctuations of the 1970s, which were only slightly larger than those of the 1940s, are associated with a dramatically higher response in precipitation, streamflow, and ΔV. The opposite phase, when ΔV and local precipition/streamflow are minimum, is associated with enhanced high pressure and a diversion of storms from

the Great Basin. The projection of the global temperature signal in the GSL region is weak, and temperature variations do not impact significantly on evaporation Thus, quasidecadal ΔV variations are driven largely by precipitation rather than evaporation changes. This is consistent with the results of analysis of at-site data reported elsewhere (5).

The position of the low pressure trough, and high pressure centers off the Pacific coast, and towards southeastern Canada are reminiscent of the PNA circulation pattern which has been connected with decadal and interdecadal climate variability elsewhere (10,17). Dynamical consistency between the temperature and P_s fields is apparent, with anomalous southerly and northerly flow on either side of the large cyclonic pressure anomaly associated with warm and cold temperature anomalies respectively. Warm anomalies off the Atlantic coast are consistent with anomalous easterly flow and decreased incidence of cold-air winter outbreaks suggested by the P_s pattern. Dynamical consistency of the P_s and global temperature patterns, along with clear statistical connections, suggests that the quasidecadal P_s variations, and their consequent impact on the at-site hydrological variations discussed above, are indeed related to *global-scale* climate variations.

On secular time scales, increasing SLB-precipitation is well correlated with the local decreasing P_s (Fig. 9). The secular temperature mode exhibits a strong warming tendency through the late 1940s. Consistent with increased evaporation, ΔV tends to decrease, until about 1940. Thereafter, increasing precipitation seems to counteract the decline and ΔV increases. The local P_s signal is associated with a large-scale pattern (Fig. 10) indicating a developing low pressure anomaly over much of the U.S., particularly in the west, implying an enhanced presence of mid-latitude storms in the region. The trough is most pronounced to the north of GSL which may lead to enhanced precipitative forcing largely from the northern part of the basin. The temperature pattern is dominated by an overall warming, but regional variations in the magnitude of warming may be associated with indicated circulation anomalies.

A compelling case can thus be made that low-frequency climatic signals drive variations in the Great Salt Lake volume on certain preferred time scales. Secular

climate variability leads to competing impacts on the lake through increasing temperatures that favor increased evaporation and changing circulation patterns that favor increased precipitation. Thus, the Great Salt Lake affords an example of how some systems may remain stationary even under a climate change scenario. On decadal time scales, quasiperiodic variations in atmospheric circulation drive lake volume variations through their effect on precipitation forcing of the lake. The associated large-scale variations in atmospheric circulation are dynamically consistent with quasidecadal global temperature variations, and may be related to climatic variability with an origin in North Atlantic ocean-atmosphere interaction. The latter variations, which describe almost 20% of the interannual variance in ΔV while not phase-coherent, may still offer prospects for improved forecasts of the Great Salt Lake volume. More generally, better forcasting of diverse hydroclimatic phenomena may be achieved through isolating the effects of low-frequency, large-scale climatic variability. Dynamical modeling of regional hydrological systems, for example, should benefit from incorporating the effects of large-scale climatic forcing in boundary conditions, and statistical forcasting/analysis techniques should benefit from making use of slowly-evolving climate and surface hydrology state variables. We hope that the present study will stimulate work in this area.

REFERENCES AND NOTES

1 Lins, H.F., *J. Clim. and Appl. Met.*, **24**, 463–471 (1985); D.R. Cayan and D.H. Peterson, *Geophys. Monogr.*, No. 55, Amer. Geophys. Union, 375–397 (1989); L.L Ely, Y. Enzel, V.R. Baker, D. R. Cayan, *Science*, **262** 410–412 (1993); E.M. Rasmusson and P.A Arkin, *J. Clim.*, **6**, 1495–1522 (1993).

2 Gridded (5^o longitude by 5^o latitude) monthly-averaged Sea Level pressure were obtained from the National Center for Atmospheric Research [R. Jenne, "Datasets for meteorological research", NCAR report TN/IA-111 (1975)] The temperature analyses are from (10) and were based on similarly gridded monthly land air and sea-surface temperature anomaly data [see P.D. Jones and K.R. Briffa, *Holocene*, **1**, 165–179 (1992)]. We use the period 1899-1990 during which both temperature and sea level data are available. The signal in the GSL region is obtained by a spatial interpolation of surrounding gridpoint values. The GSL, SLB, and BFH records are described in (5). SLB was selected since it is the highest elevation long-record precipitation station in the GSL basin. Precipitation increases dramatically with elevation, and hence SLB is a good index of precipitation driving the GSL. BFH is the longest record of streamflow which enters into the GSL that is free of regulation or diversion. SLB and BFH are located near the south and north ends, respectively, of the GSL basin, providing an estimate of spatial variability of the hydrological forcing.

3 For each grid point m we remove the long-term mean, and normalize by the long-term standard deviation $\sigma^{(m)}$ to yield the time series ${x_n}^{(m)}$ ($n = 1, \ldots, N$ months).

Using the set of normalized time series, we transform from the time to spectral domain using the multitaper spectral representation,

$$ {Y_k}^{(m)}(f) = \sum_{n=1}^{N} w_n^{(k)} {x_n}^{(m)} e^{i2\pi f n \Delta t} \qquad (1) $$

where $\Delta t = 1$ month is the sampling interval and $\{w_n^{(k)}\}_{n=1}^{N}$ is the kth member in an orthogonal sequence of Slepian tapers [D.J. Thomson, *IEEE Proc.*, **70**,

1055–1096 (1982)]. A given spectral estimate averages in the frequency band $f \pm p/N\Delta t$. We use $K = 3$ tapers with bandwidth $2f_R$ where $f_R = 1/N\Delta t$ to optimize the separation of distinct signals in the frequency domain. For the 92 year length series, the 2π tapers average over a half bandwidth of $2f_R = 0.02$ cyc/yr.

Using the K Multitaper spectra at a given frequency f for each of the M grid points, we construct the matrix,

$$\mathbf{A}(f) = \begin{bmatrix} Y_1^{(1)} & Y_2^{(1)} & \dots & Y_K^{(1)} \\ Y_1^{(2)} & Y_2^{(2)} & \dots & Y_K^{(2)} \\ \vdots & & & \\ Y_1^{(M)} & Y_2^{(M)} & \dots & Y_K^{(M)} \end{bmatrix} \tag{1}$$

$\mathbf{A}$ is decomposed by a complex-valued SVD into K orthonormal spatial left-eigenvectors $\mathbf{u}_k$ and K orthonormal spectral right-eigenvectors $\mathbf{v}_k$. For each mode k, a singular value λ_k describes the variance described by that mode in the decomposition.

The $\mathbf{v}_k$ can be inverted with additional constraints to obtain the slowly-varying time envelope of the kth mode at frequency f. The $\mathbf{u}_k$ determine the spatial patterns of the oscillation corresponding to frequency f (amplitude and relative temporal phase among grid points). The components of $\mathbf{u}_k$ are rescaled by the monthly standard deviations σ_m to restore proper units. These spatial patterns are projected onto a chosen phase in a typical cycle to yield a real-valued pattern of positive and negative anomalies (e.g., we can set the phase at the GSL to zero and recover the corresponding spatial pattern when the projection is maximum there).

In order to test the significance of the spatiotemporal modes identified, we performed 1000 Monte Carlo realizations with a white-noise process locally in the frequency domain, with $k = 2, \dots, K$ spectral degrees of freedom and and $\tilde{M}$ spatial degrees of freedom. We estimate the number of spatial degrees of freedom $\tilde{M}$ in the data sets by determining a rough near-neighbor correlation length, yielding $\tilde{M} \sim 8$ among the 69 U.S P_s gridpoints. Any λ_k that garners

a larger fractional variance than the λ_k in 95% of the Monte Carlo simulations is taken to be statistically significant. Since the SVD analysis is performed locally within narrow frequency bands throughout the frequency domain, this null-hypothesis is justified as long as the background spectral amplitudes of the individual gridpoint time series do not vary rapidly over the frequency bandwidth of the Slepian tapers. Overall, the time series analyzed here satisfy this assumption. A similar test was used to establish the significance of global temperature modes discussed in the present study (10).

4 We identify the oscillation $y(t)$ centered near frequency f_0 in a given time series by a Multitaper envelope method [J. Park and K. A. Maasch, *J. Geophys. Res.*, **98**, 447–461 (1993)] by which we model quasiperiodic processes by an oscillation centered at f_0 that is phase or amplitude modulated on a longer time scale by an slowly-varying envelope function E(t), such that $y(t) = E(t)\cos(f_0 t + \phi)$. Since $E(t)$ is slowly-varying, it is well described by a small number of spectral degrees of freedom K. We use $K = 3$ for consistency with our description of large-scale quasiperiodic modes in the gridded data fields.

5 U. Lall and M.E, Mann, Eos **74**, 123 (1993); U. Lall, M.E. Mann, B. Saltzman, in preparation.

6 Lall, U. and Y. Moon, Eos **75**, 21, (1994).

7 K. Labitzke and H. van Loon, *J. Atmos. Terr. Phys.*, **50**, 197–206 (1988).

8 R.G. Currie and D.P. O'Brien, *Int. J. Climatol.*, **12**, 281–304 (1992).

9 H.C. Willett and J.T. Prohaska, *Cenezoic Geology of Western Utah-Sites for precious metal and hydrocarbon assimilations*, Utah Geol. Assoc., pub. 16 (Salt Lake City, 1987).

10 Mann, M.E., and J. Park, *Proceedings of the 6th Conference on Climate Variations*, Jan. 1994 (American Meteorological Society, Nashville 1994)

11 C. Deser and M. Blackmon, *J. Clim., 6*, 1743–1753, 1993.

12 M.D. Dettinger and M. Ghil, *Proc. XVIth annual climate diagnostics workshop*, U.S. Department of Commerce, NOAA (Los Angeles, 1991).

13 A.K Guetter and K.P Georgakakos, *Bull. Am. Met. Soc.*, **74**, 1873–1891 (1993).

14 G.E. Bingham, E.A. Richardson, G.A. Ashcroft; and J.K. Eischeid, R.S. Bradley, X. Shao, *Problems and Prospects for predicting Great Salt Lake levels*, P. Kay and H.F. Diaz, Eds. (Salt Lake City, 1985).

15 We measure correlation between two records on a given time scale using the multitaper spectral coherence [M.E. Mann and J. Park, *Geophys. Res. Lett.*, **20**, 1055–1058 (1993)]. The spectral coherence $C(f)$ measures the similarity between the slowly-varying envelopes of oscillations at the same frequency. As each oscillation in this study is described by $K = 3$ complex spectral degrees of freedom, the significance of the squared-coherence is related to an F-test with 2 and 4 degrees of freedom [D.R. Brillinger, *Time Series, Data Analysis and Theory*, (McGraw-Hill, New York, ed. 2, 1981), pp. 313-317.] The 99%, 95% and 90% confidence levels for $|C(f)|^2$ are 0.90, 0.78, and 0.68 respectively, while the median of the distribution is 0.29.

16 L. Benson and R.S. Thompson, *The physical record of lakes in the Great Basin*, W.F. Ruddiman and H.E. Wright Jr., Eds., Geological Society of America, (Boulder, 1987).

17 K.E. Trenberth, *Bull. Am. Met. Soc.*, **71**, 988–993 (1990).

18 Supported by the Division of Atmospheric Sciences (Climate Dynamics Program) of the National Science Foundation under grant ATM-9222591 at Yale University and NASA grant NAG5-2316 (to M.E.M and B.S.), and NSF grant EAR-9205727 and USGS grant 1434-92-G-226 (to U.L.).

Figure Captions

FIG. 1

Great Salt Lake volume (V) monthly time series (in units of m^3) from 1899-1991. While the annual cycle is the most regular feature in the record, the decadal/interdecadal variability is considerably higher in amplitude.

FIG. 2

Location of GSL and relevant at-site hydrology/weather stations.

FIG. 3

Fractional variance explained by the first eigenvalue of the SVD as a function of frequency in cycle/year for the U.S. P_s data set. Horizontal dashed lines denote 90%,95%, and 99% confidence limits from Monte Carlo simulations. Analysis is performed seperately using all months (solid), winter (DJF-dashed), and summer (JJA-not shown) seasons. Sampling fluctuations are more problematic in the seasonal analyses since there is a small ensemble of winter and summer averages. Significant peaks based on all months are found in the secular band (which averages on time scales greater than 46 years), a 20-26 yr interdecadal band, the 10-12 year quasidecadal band and interannual bands which may be associated with ENSO and quasibiennial processes. These peaks are robust with respect to performing the analysis dropping the first/last 10 years of data. The secular and quasidecadal peaks are observed during all seasons, while the interdecadal variations are distinctly a summer phenomenon. All but the latter peak are observed in the SVD variance spectrum resulting from a similar previous analysis of gridded global surface temperature anomaly data (10), the results of which are utilized in this study.

FIG. 4

(a) GSL monthly differenced record (ΔV), lowpassed at 2 year frequency to show interannual and longer time scale variability, along with reconstructed signal using secular, and quasi-decadal ($\sim$11 year) components (units are m^3/month). The secular component explains a modest 1.5% of the total interannual variance of the ΔV record, while the quasidecadal component explains a more sizeable $\sim$ 18%. The large fluctu-

ations of the 1980s may be associated with constructive interference of quasidecadal and interannual oscillations.

FIG. 5

Multitaper reconstructions (4) of quasidecadal variations in ΔV (solid, in units of $2.5 \cdot 10^8$ m^3/month) and annual sunspot numbers (dashed-vertical scale normalized to plot dimension). The spectral coherence ($C^2 = 0.03$) between the two records in this frequency band is not even significant at the 50% level (15). The two signals clearly drift in phase relative to each other, and are not similarly amplitude modulated. The same holds for all of the other records analyzed with respect to sunspot variations.

FIG. 6

Quasidecadal U.S. P_s mode (dashed) in units of millibars (mb) and global temperature modes (solid) projected onto GSL region. The temperature oscillation (shown in units of 0.01°C) nearly vanishes locally in the GSL region (the spatial pattern of the signal is shown below), but is considerably higher-amplitude elsewhere in the U.S. Positive P_s anomalies are lagged about 90-110° in phase relative to (small) positive temperature anomalies locally.

FIG. 7

Quasidecadal variations in

a) ΔV (solid–units of $2.5 \cdot 10^8$ m^3/month), SLB-precipitation (dashed, units of 2.5 mm/month), and BFH streamflow (dot-dashed, in units of 1.5 m^3/s).

b) SLB precipitation (solid, same units as above) and local projection of quasidecadal P_s mode (dashed, units of mb)

Each of the above signals are mutually correlated at greather than $> 95\%$ confidence levels (15). Similar amplitude modulation and relatively constant phase-relationships are observed obetween different records, except when the envelopes pass near or through zero amplitude at which time background noise may obscure the underlying signals. Phase discontinuities are observed during the 1930s and near 1960 in each record, but the oscillations are otherwise reasonably phase-coherent. The phase-discontinuity near 1960 is also observed in interdecadal temperature oscillations of $\sim$16-18 year period (10).

FIG. 8

Large-scale quasidecadal climate pattern when precipitation and ΔV are maximum at GSL. Position of GSL is indicated by a small rectangle with the approximate dimensions of the lake. P_s is contoured in units of millibars (mb) with a peak-to-peak pattern amplitude of about 1.2 mb in this case. The silmultaneous projection of the quasidecadal global temperature mode (10) is shown with arrows proportional to peak-to-peak magnitude of anomaly. Rightward arrows indicate warm anomalies, while leftward arrows denote cold anomalies. Pattern maximum amplitude is $\sim 0.6°$C, with low-amplitude in the GSL region. It is worth noting that the temperature pattern largely cancels when averaged over the U.S.

FIG. 9

Secular trends of ΔV (dotted, units of $2.5 \cdot 10^8$ m^3/month), SLB-precipitation (dashed, units of 2.5mm/month), and secular P_s (dot-dashed, mb) and temperature (solid, °C) modes projected onto GSL region.

FIG. 10

Large-scale pattern of secular modes. Pattern peak amplitude is -3.3 mb northeast of the GSL. Temperature trends are indicated by same convention as above, showing a spatially-varying warming trend. Maximum amplitude warming in the pattern is $0.85°$C off the mid-Atlantic coast, with moderate $\sim 0.4 - 0.5°$C warming over much of the great basin.

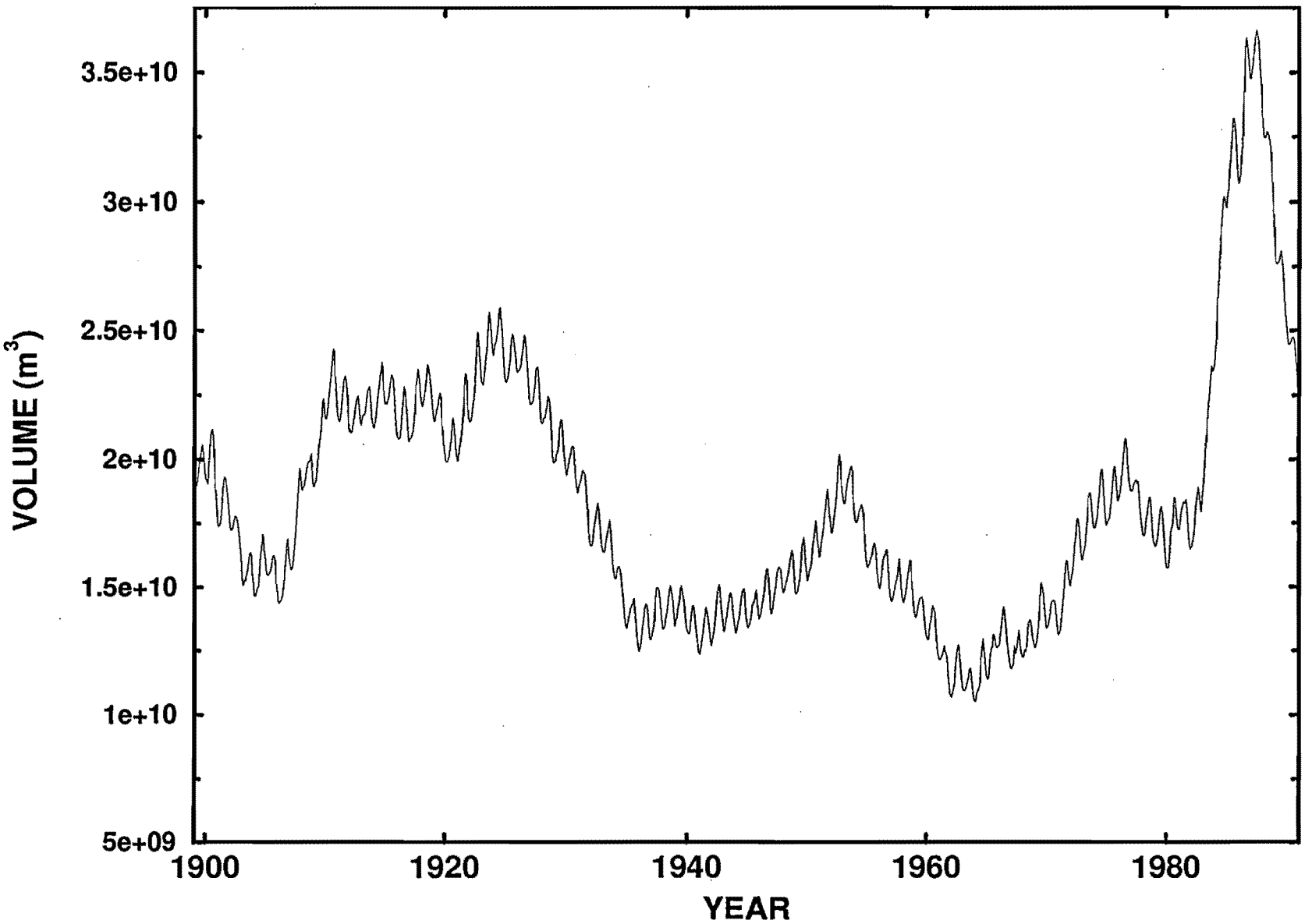
3.5e+10
3e+10
2.5e+10
2e+10
1.5e+10
1e+10
5e+09
VOLUME (m3)
1900
1920
1940
1960
1980
YEAR

Fig. 1

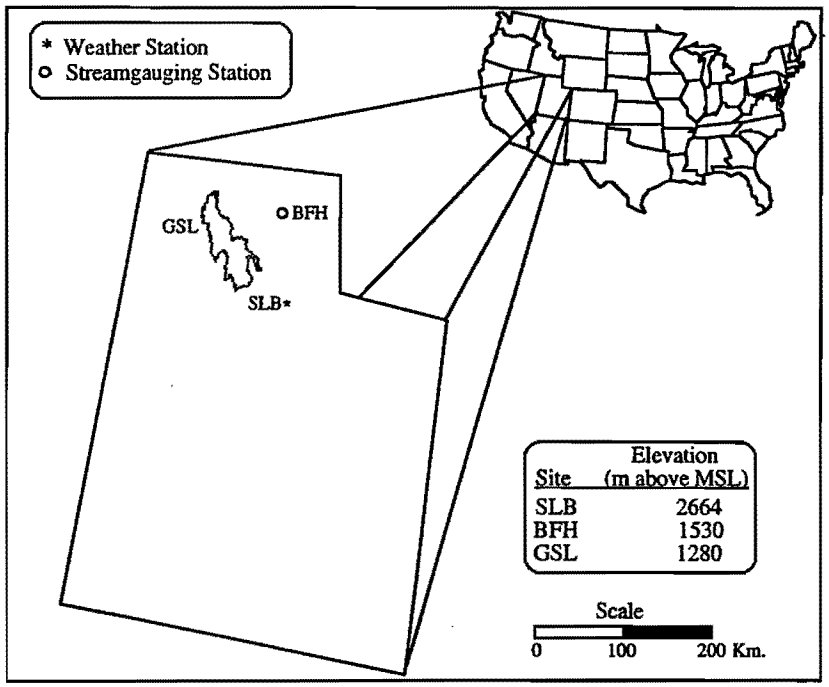
* Weather Station
o Streamgauging Station
GSL
o BFH
SLB*
Site
Elevation (m above MSL)
SLB 2664
BFH 1530
GSL 1280
Scale
0 100 200 Km.

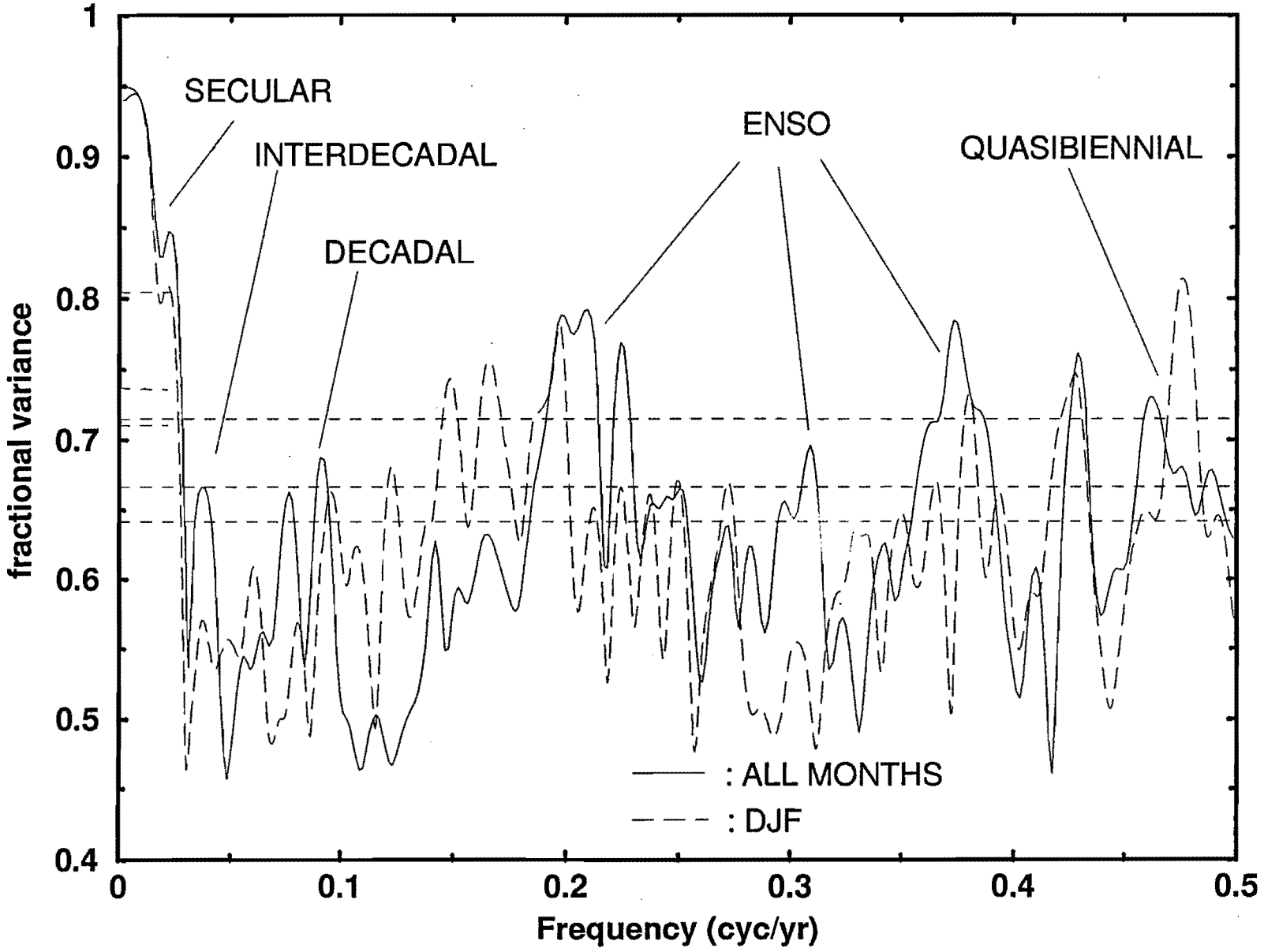
SECULAR
INTERDECADAL
DECADAL
ENSO
QUASIBIENNIAL
: ALL MONTHS
: DJF
fractional variance
Frequency (cyc/yr)
1
0.9
0.8
0.7
0.6
0.5
0.4
0
0.1
0.2
0.3
0.4
0.5

Fig. 3

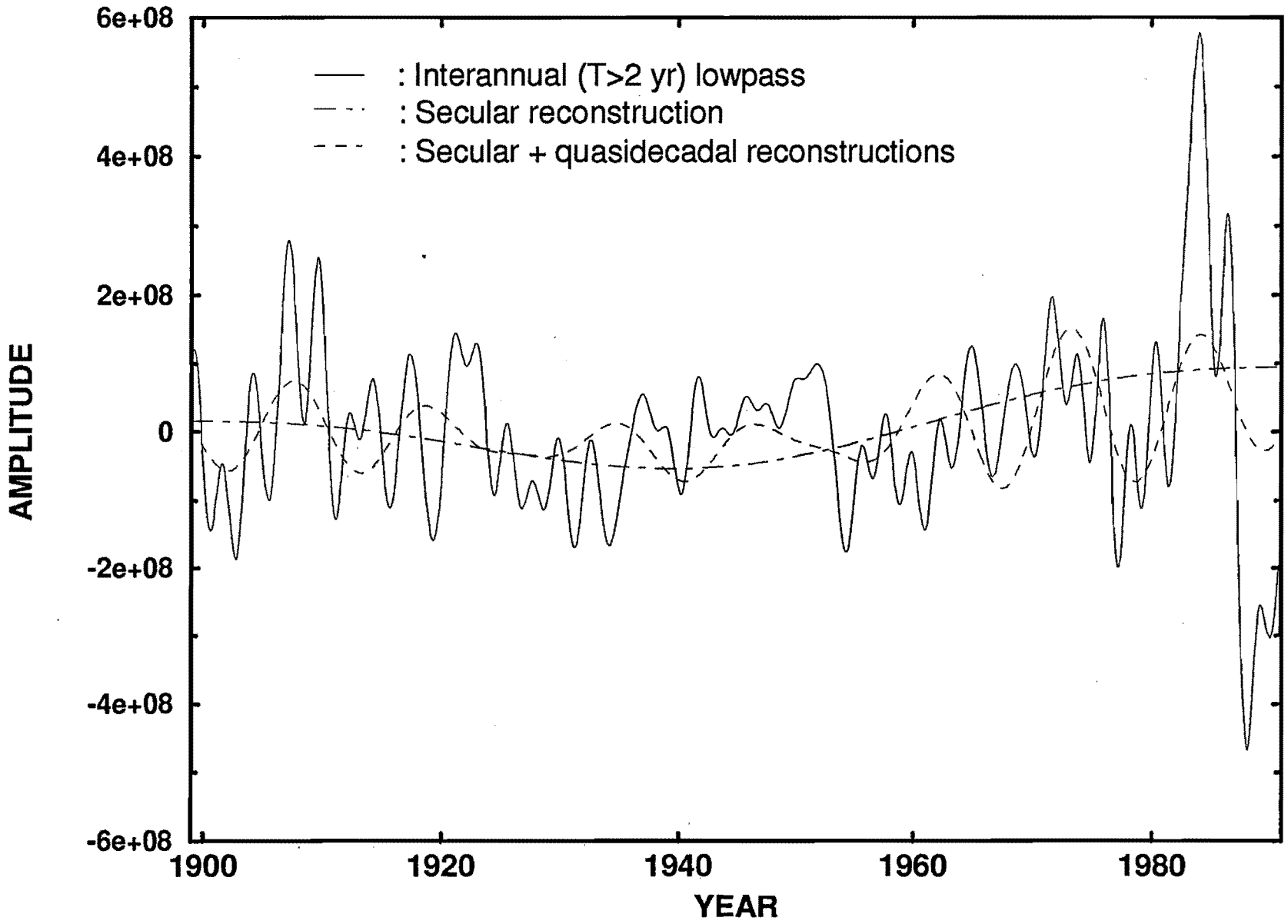
6e+08
4e+08
2e+08
0
-2e+08
-4e+08
-6e+08
AMPLITUDE
1900
1920
1940
1960
1980
YEAR
: Interannual (T>2 yr) lowpass
: Secular reconstruction
: Secular + quasidecadal reconstructions

Fig. 14

Fig. 5

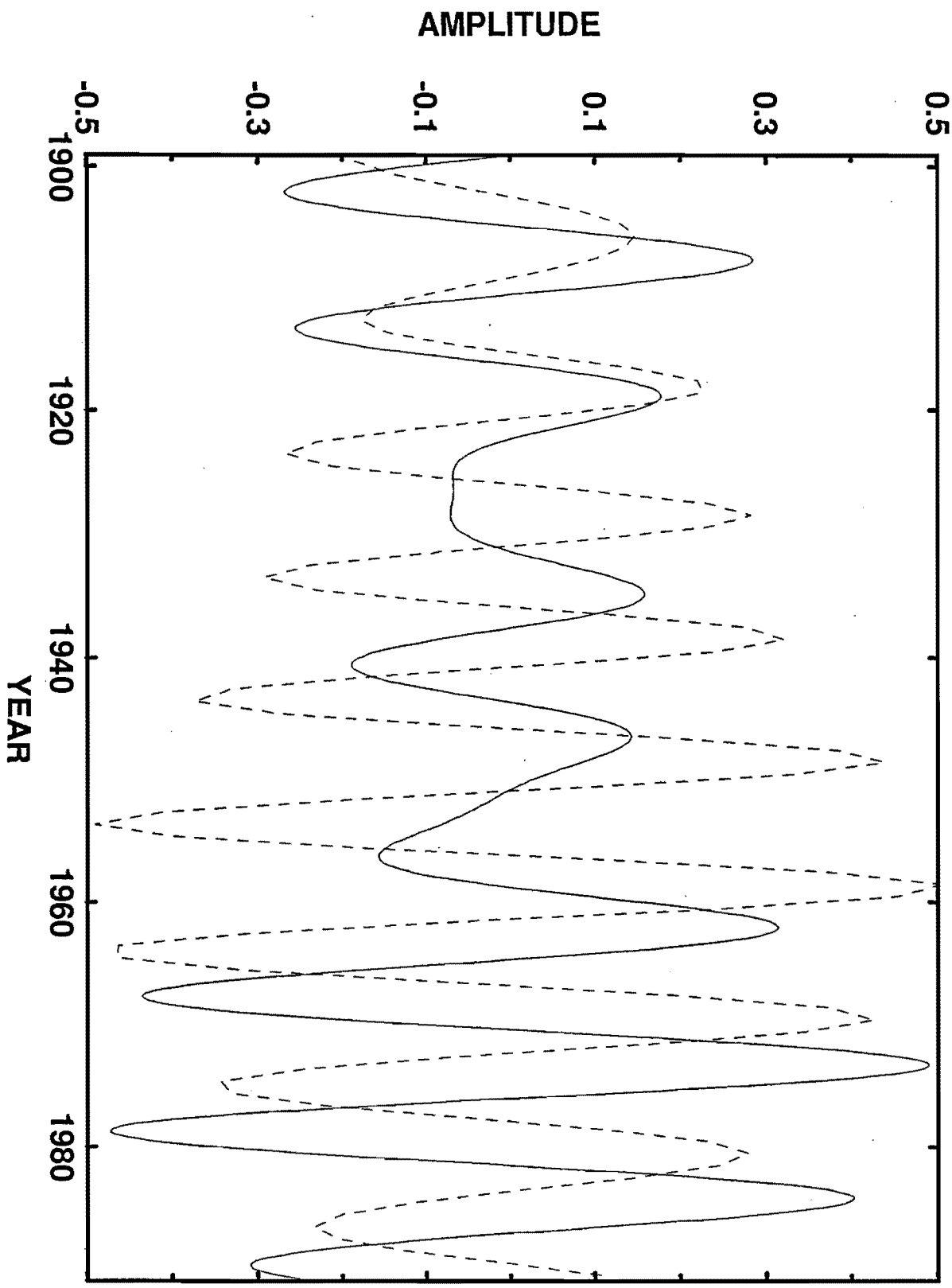

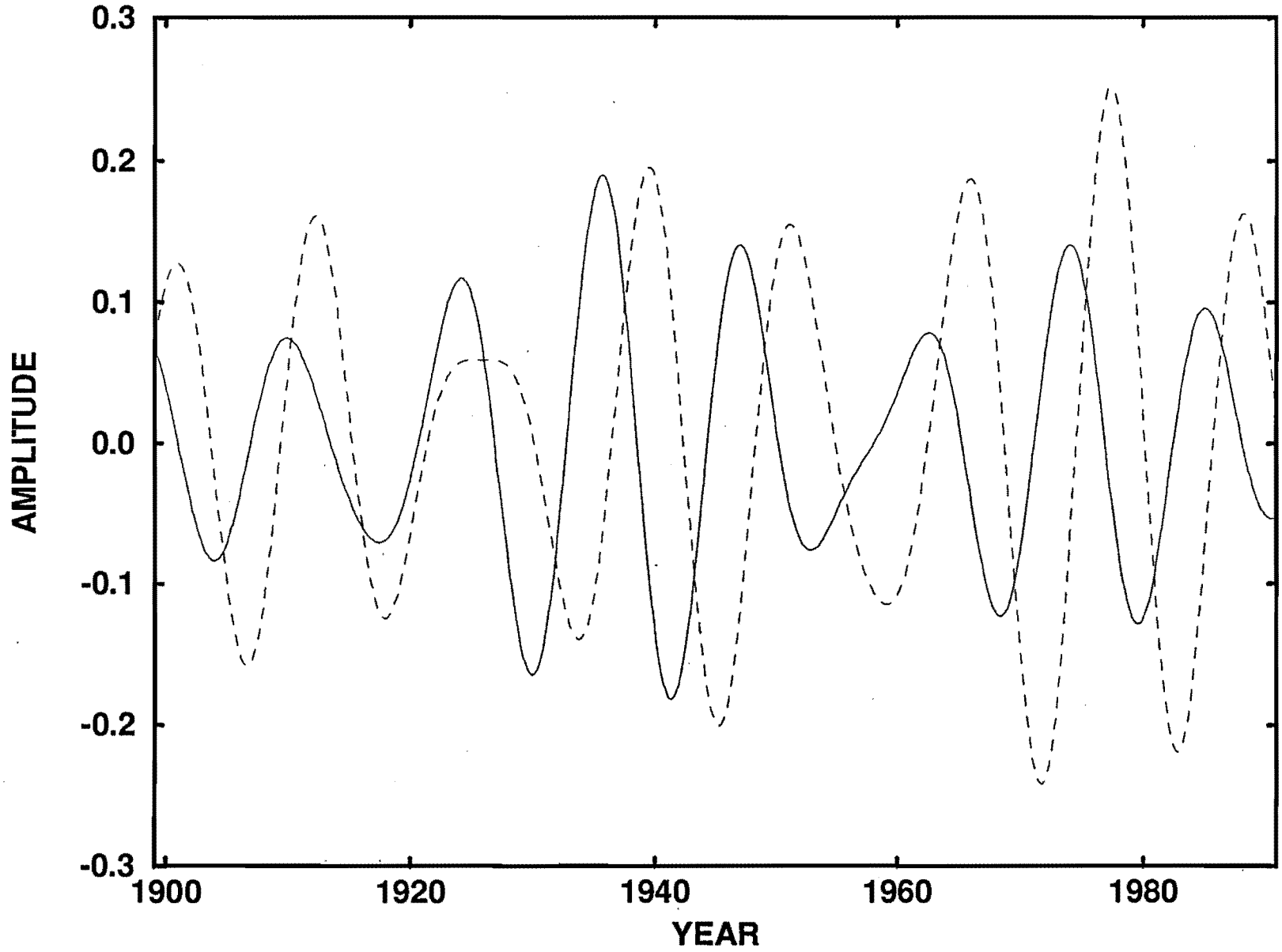

Fig. 6

Fig 7a

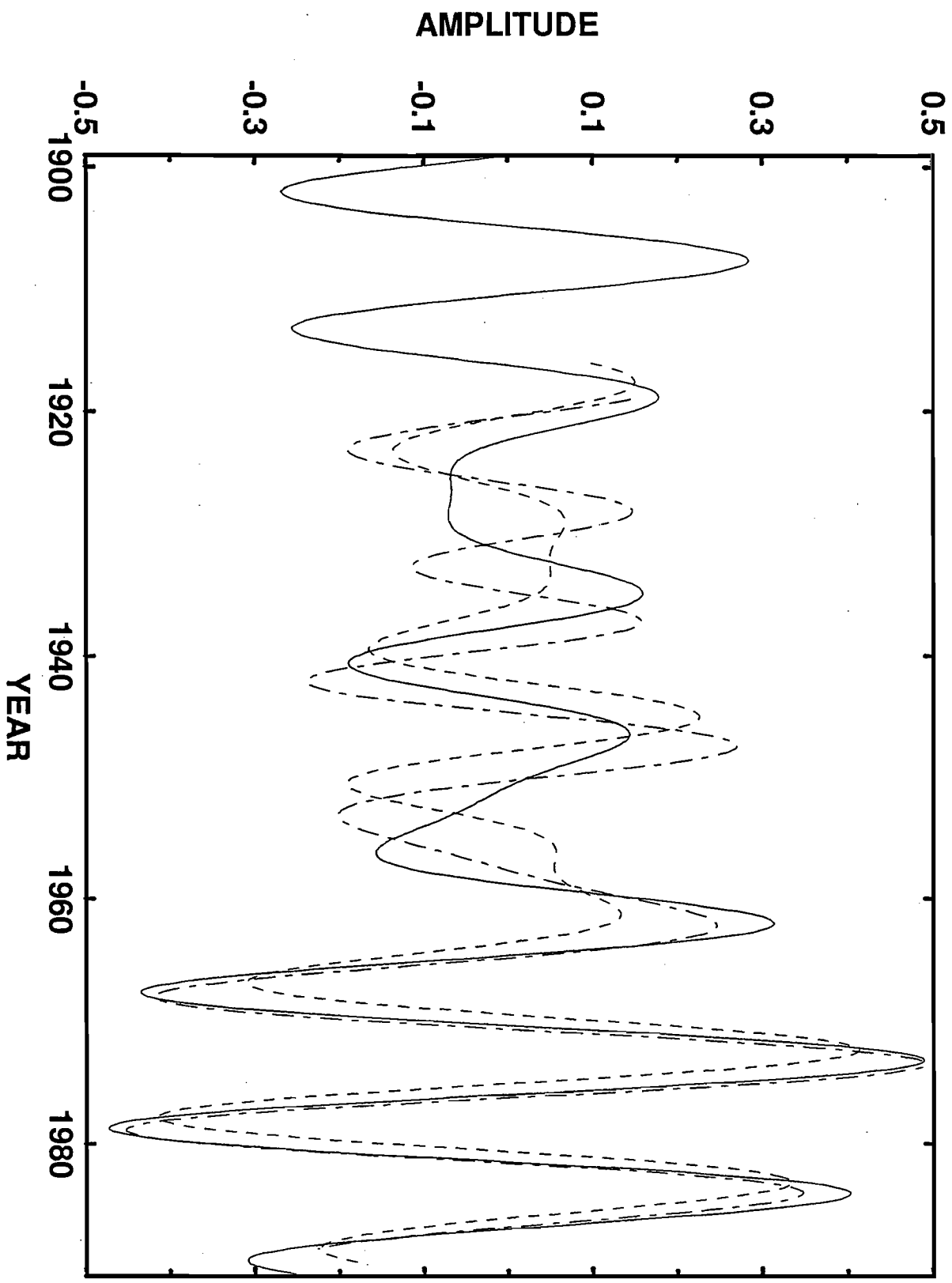

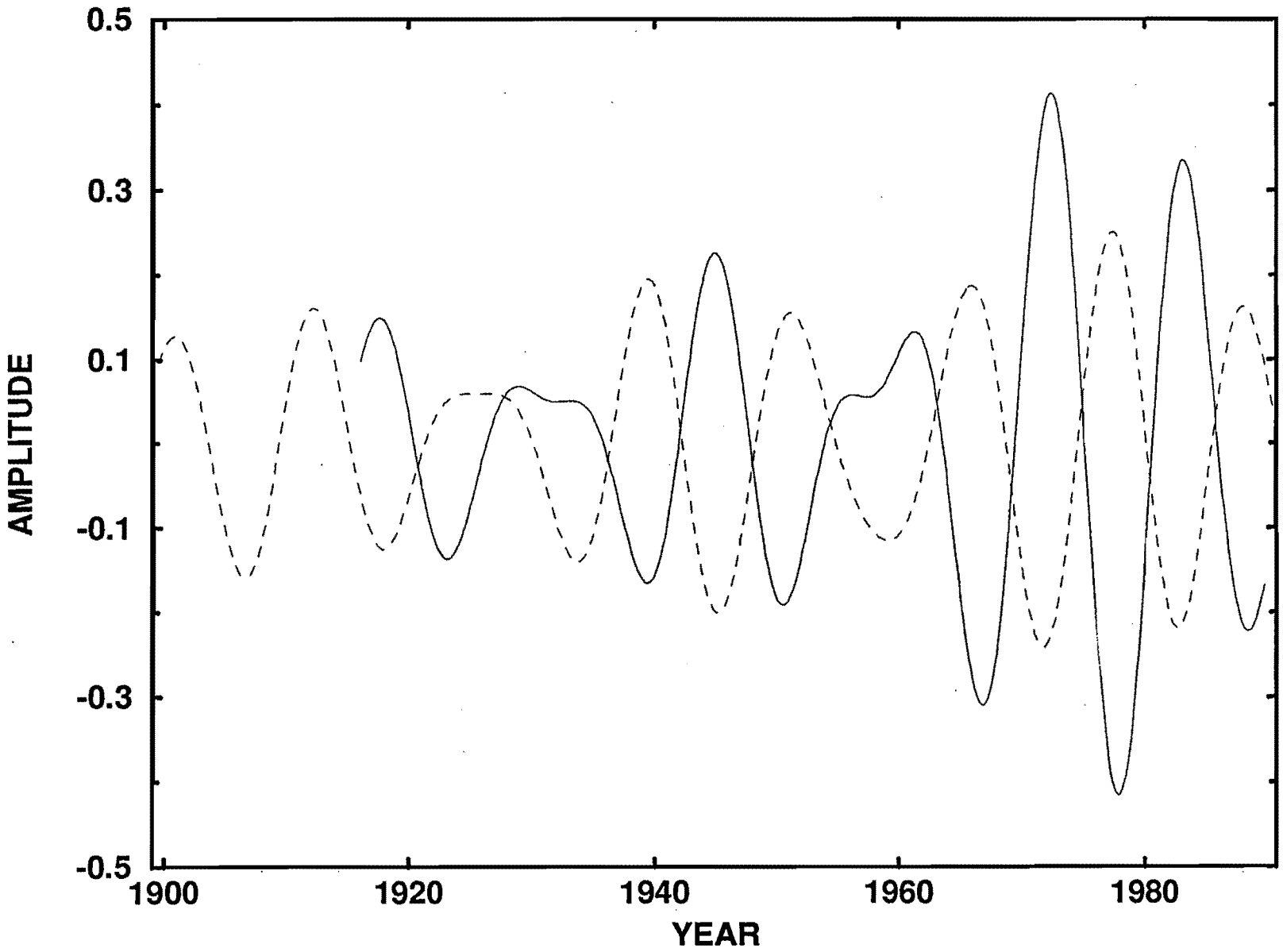

Fig 7b

QUASIDECADAL

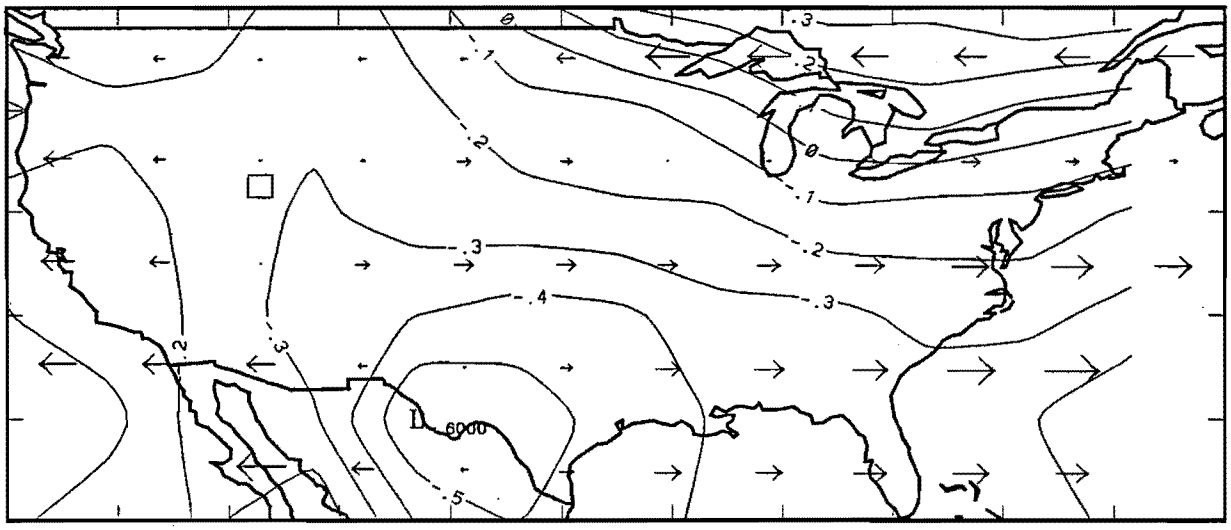

CONTOUR FROM −.5 TO .3 BY .1

Fig. 8

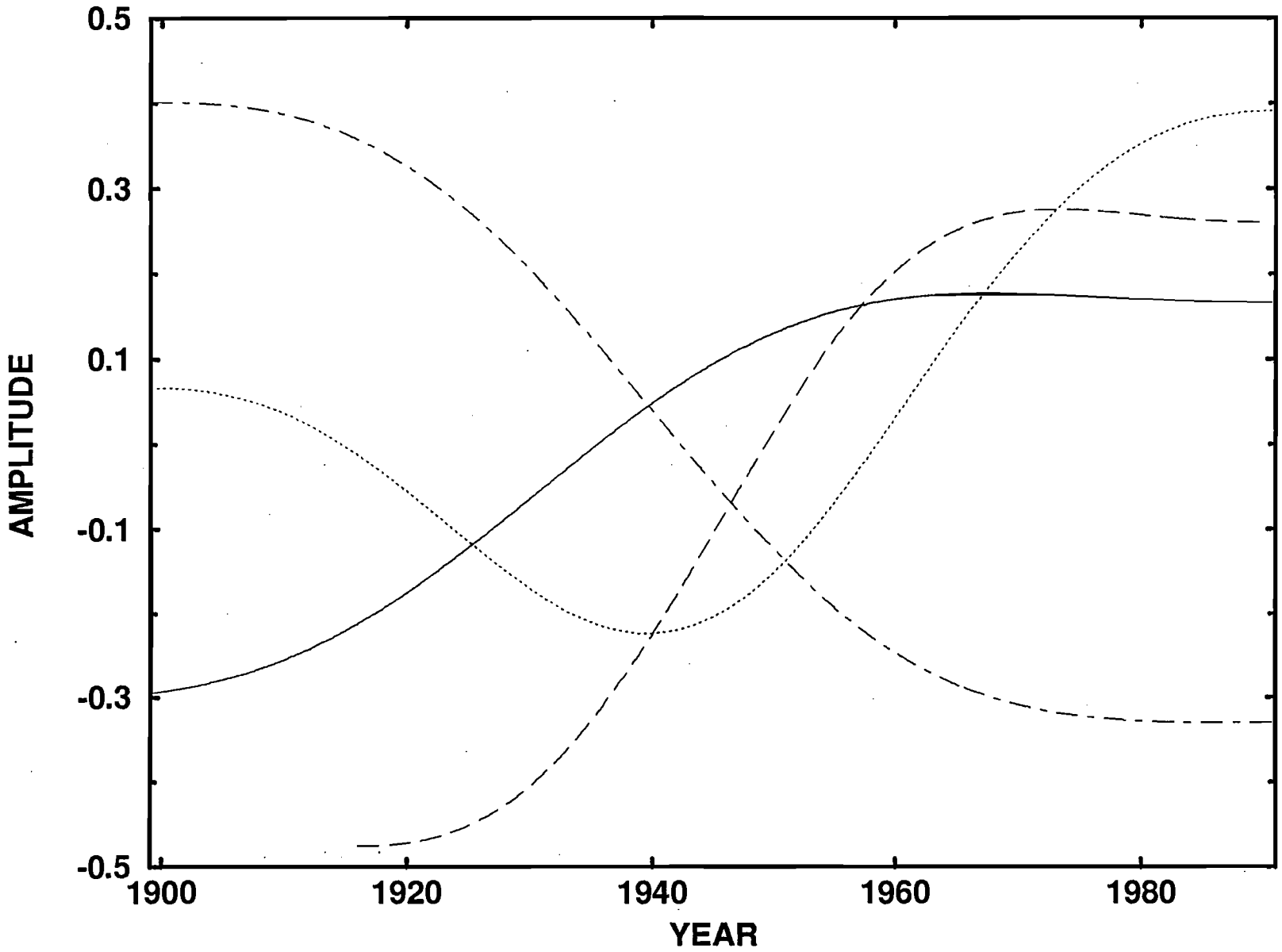

Fig. 9

SECULAR TREND

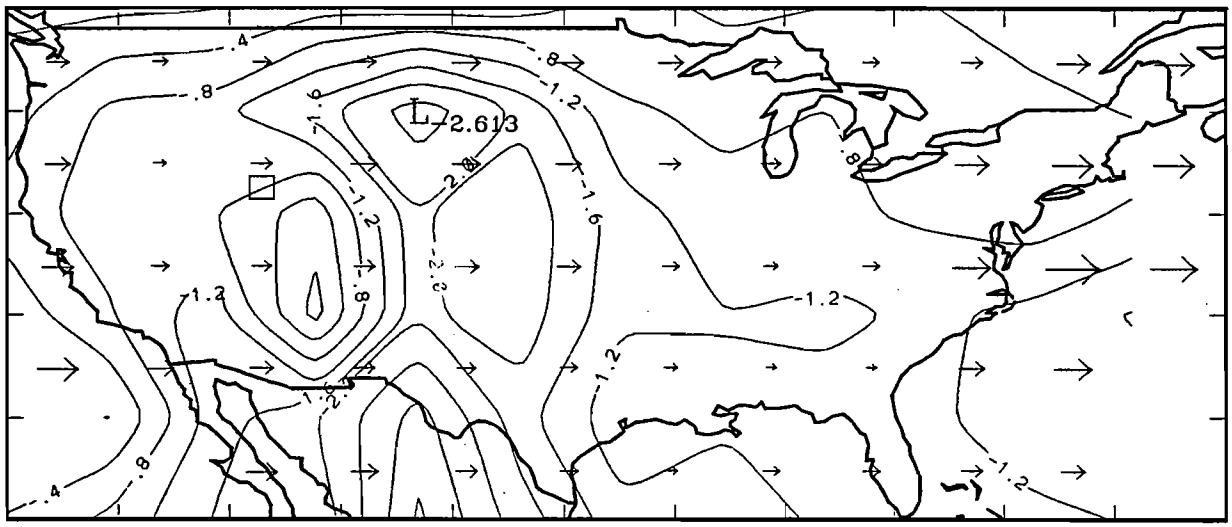

CONTOUR FROM −3.2 TO 0 BY .4

Fig.10